J Mater Sci (2011) 46:7152–7159
DOI 10.1007/s10853-011-5647-9

SIZE DEPENDENT EFFECTS

Effect of Co and Ce on silica supported manganese catalysts in the reactions of complete oxidation of *n*-hexane and ethyl acetate

S. Todorova · A. Naydenov · H. Kolev · K. Tenchev · G. Ivanov · G. Kadinov

Received: 19 December 2010 / Accepted: 17 May 2011 / Published online: 1 June 2011

Abstract Mono-component and bi-component catalysts, prepared by impregnation of silica with aqueous solution of Mn, Co, and Ce nitrates, were tested in the reactions of complete oxidation of *n*-hexane and ethyl acetate. The catalysts were characterized by powder X-ray diffraction, temperature-programmed reduction, X-ray photoelectron spectroscopy, and Fourier transform infrared spectroscopy (FTIR). The catalytic activity is significantly increased by the combination between manganese and cobalt, which is explained as a result of the high mobility of lattice oxygen, the simultaneous presence of Mn^{4+}–Mn^{3+} couple, decrease in the strength of the Co–O bond, and the predominance of Co in the second oxidation state on the catalyst surface. The decrease in catalytic activity of Mn–Ce sample is attributed to the predominance of Ce on the surface and lower mobility of the lattice oxygen.

Introduction

Volatile organic compounds (VOCs) are known to contribute to a number of environmental problems such as formation of ground-level ozone, photochemical smog, and toxic air emissions [1]. When there is no interest in recovering VOC, they are usually destroyed by deep oxidation. Among the techniques to decompose VOC, catalytic oxidation is preferable to thermal oxidation because of its low energy consumption and lower temperature of operation. Catalysts based on precious metals are commonly used for these processes. Metal oxides are an alternative to the high cost noble metals. Among all studied metal oxides, the most active single oxides are those of Cu, Co, Mn, and Ni. The catalytic properties of MnO_x-based catalysts are attributed to the ability of manganese to form oxides with different oxidation states and to the high mobility of oxygen species [2, 3].

Cobalt oxide is reported to be quite promising among the metal oxides used for preparation of supported catalysts for the removal of CO [4–6] and VOC [7–9]. The active phase dispersion in supported catalysts is known to control their activity. In our previous investigations, we found [10] a considerable increase in activity with the samples prepared from mixed solution of $Co(NO_3)_2{\cdot}6H_2O$ and $Mn(NO_3)_2{\cdot}6H_2O$ irrespective of the Co/Mn ratio, when compared with the samples, prepared by consecutive impregnation of the metal salts. This was related to the formation of finely divided oxides upon combination between cobalt and manganese. Cerium has high oxygen storage capacity, associated with fast Ce^{4+}/Ce^{3+} redox process, ensuring more oxygen available for the oxidation process. MnO_x–CeO_2 catalysts have been tested in the oxidation of different VOCs as ethanol, formaldehyde, and hexane [11–13].

It is of interest to compare the effect of Co and Ce additives on the catalytic activity of supported manganese catalysts in the reaction of complete oxidation of ethyl acetate and *n*-hexane, especially when both the bicomponent samples (Mn–Co and Mn–Ce) are prepared using a mixed aqueous solution of the respective salts. *n*-Hexane was chosen as a representative VOC of saturated aliphatic hydrocarbons and ethyl acetate of esters, both compounds being widely used in the industry.

S. Todorova (✉) · H. Kolev · K. Tenchev · G. Kadinov
Institute of Catalysis, Bulgarian Academy of Sciences, Acad. G. Bonchev St., Bldg. 11, 1113 Sofia, Bulgaria
e-mail: todorova@ic.bas.bg

A. Naydenov · G. Ivanov
Institute of General and Inorganic Chemistry, Bulgarian Academy of Sciences, Acad. G. Bonchev St., Bldg. 11, 1113 Sofia, Bulgaria

Experimental

Catalyst preparation

Single component (Co and Mn) and bi-component (Mn-Co and Mn–Ce) samples were prepared by introduction of silica (Aerosil $S_{BET} = 147\ m^2/g$) to an aqueous solution of the respective salts $Mn(NO_3)_2{\cdot}6H_2O$, $Co(NO_3)_2{\cdot}6H_2O$, and $Ce(NO_3)_2{\cdot}6H_2O$. To prepare the catalysts, the target amount of salt aimed at obtaining the desired content of metal (~12% metal) was diluted in 35 mL of distilled water under stirring at room temperature until complete dissolution and then 2.5 g of silica was added. The slurry was further stirred 1 h at 333 K, evaporated under vacuum at the same temperature. The bi-component samples (Mn–Co, Mn–Ce) were obtained from a mixed aqueous solution of the respective salts. All samples are calcined for 2 h at 450 °C. The metal content in the samples was about 12 wt% (12 wt% Mn/SiO_2, 6 wt% Mn + 6 wt% Co/SiO_2, and 7 wt% Mn + 7 wt% Ce/SiO_2, respectively). Some general characterization data of the samples are given in Table 1.

Catalysts characterization

Powder X-ray diffraction (XRD) patterns were collected at room temperature in a step-scan regime (step = 0.04°) on a Bruker D8 Advance diffractometer using Cu K_α radiation. XRD data processing was performed using the X'Pert HighScore program. The amount of manganese and cobalt in the catalysts was determined by inductively coupled plasma-atomic emission spectroscopy (ICP-AES) (ARL 3410).

Temperature-programmed reduction (TPR) was carried out in an equipment described elsewhere [14], using a flow mixture 10% H_2 in Ar at 10 mL/min, temperature ramp of 10 °C/min to 700 °C. Prior to the TPR experiment, the samples were treated in Ar for 30 min at 150 °C.

The X-ray photoelectron spectroscopy (XPS) measurements were carried out in the UHV chamber of an ESCALAB-MkII (VG Scientific) electron spectrometer with a base pressure of about 1×10^{-10} mbar (during the measurement 1×10^{-9} mbar). The photoelectron spectra were obtained using unmonochromatized Al K_α (hv = 1486.6 eV) radiation. Passing through a 6-mm slit (entrance/exit) of a hemispherical analyzer, electrons with energy of 20 eV were detected by a channeltron. The instrumental resolution measured as the full width at half maximum (FWHM) of the $Ag3d_{5/2}$ photoelectron peak was about 1 eV. The energy scale was corrected to the C1s-peak maximum at 285.0 eV for electrostatic sample charging. Fitting of the recorded XPS spectra was performed, using a symmetrical Gauss–Lorentzian curve fitting after Shirley-type subtraction of the background. IR spectra were collected on a Nicolet 6700 FTIR spectrophotometer with a spectral resolution of 4 cm^{-1}, using a KBr pellet technique. The IR spectra are shown after baseline correction.

Catalytic measurements

The catalytic tests were carried out in a flow type quartz-glass reactor (reactor diameter 6.0 mm) at atmospheric pressure with a catalyst loading of about 1.0 cm^3 (sieve fraction 0.31–0.63 mm). External mass transfer limitations were minimized by working at GHSV of 30,000 h^{-1}. The reaction temperature was kept within the limits of ±1 °C, measured at the inlet and outlet of the catalyst bed.

The inlet concentrations of reactants were varied as follows: *n*-hexane 360 ppm; ethyl acetate 500 ppm, oxygen 21 vol.%; all gas mixtures were balanced to 100% with nitrogen. The gas analysis of reaction products was performed using on-line analyzers for $CO/CO_2/O_2$ (Maihak) and total hydrocarbons content (THC, ThermoFID).

Results and discussion

The XRD patterns of the mono- and bi-component samples are shown in Fig. 1. The XRD characteristic of Mn sample was described in our previous investigation [10]. The XRD spectrum of mono-component manganese sample shows

Table 1 Sample characterization

Sample	Metal content (wt%)			Surface composition[c] (at.%)			Atomic Mn/Co and Mn/Ce ratio	
	Co	Mn	Ce	Co	Mn	Ce	On the surface[c]	In the bulk
Mn		12.67			0.58			
Mn–Ce		7.5[b]	7.5[b]		0.44	0.38	Mn/Ce = 1.16	Mn/Ce = 2.22
Mn–Co	6.08[a]	6.2[a]		0.5	0.4		Mn/Co = 0.8	Mn/Co = 1.07

[a] From elemental analysis

[b] Metal content calculated to be supplied by the starting solutions

[c] From XPS

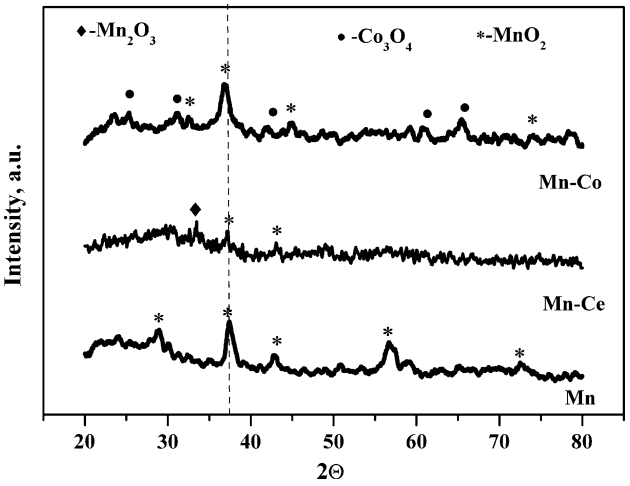

Fig. 1 XRD patterns of all studied samples calcined at 450 °C

diffraction lines at $2\theta = 28.9$, 37.3, 42.8, and 56.8 corresponding to the β-MnO_2 (PDF-00-004-0779, pyrolusite). According to literature data [15–17], bulk manganese oxides manifest different crystalline phases, depending mainly on the applied temperature and on the atmosphere during calcination. The manganese(IV) oxides are formed at low temperatures [15]. The most stable structure is β-MnO_2 [17]. The mean particles sizes of MnO_2 in the mono-component Mn catalyst, calculated according to the Scherrer equation and using the broadening of the (211) lines, are 16 nm. The broad peaks of low intensity in XRD patterns of the manganese samples modified with Co or Ce indicate the presence of very small metal oxide particles, most likely as result of the interaction between MnO_2 and additive (Co_3O_4, CeO_2) and possible formation of solid solutions. The signal at $2\theta = 33°$ in the diffractogram of Mn–Ce sample indicates the presence of α-Mn_2O_3. Additionally, the broad and poorly resolved peak in the range $2\theta = 37$–39° could be result of the presence of a mixture of Mn^{4+} and Mn^{3+} oxides [18, 19]. No cerium oxide phase was detected by XRD. Formation of a solid solution between Mn_2O_3 and CeO_2 has been previously reported for catalysts prepared by different methods [11, 20, 21], and it is attributed to structural similarities of these two phases.

The presence of cobalt in the calcined Mn-Co sample results in a shift of the main diffraction line of MnO_2 to smaller angle. Since Co and Mn have similar ionic radius, the above-mentioned change could be regarded as direct proof of dissolution of the Co ions in the lattice of MnO_2. The formation of mixed Mn–$Co_2O_{4.5}$ [22, 23] oxides has been previously reported. The analysis of XRD data on Co–Mn samples is difficult because MnO_2, Co_3O_4, and Mn–$Co_2O_{4.5}$ compounds demonstrate lines in XRD patterns at similar 2θ values [10]. The oxide particles' size in the Mn–Co sample (7 nm) was calculated from the reflection at $2\theta = 37.7$. This is not an authentic reflection of MnO_2 because several compounds present simultaneously on the support that have XRD patterns at this position. For this reason, the calculated particles size is only tentative.

Infrared spectroscopy is often a necessary alternative and useful supplement to XRD, because IR spectrum analysis is sensitive to amorphous components and those with short-range order [24]. Bands in Fourier transform infrared spectroscopy (FTIR) spectra of manganese oxides appear in the regions 200–450, 450–600, and 600–750 cm^{-1}. They correspond to spectral domains where wagging, bending, and stretching vibrations are active, respectively [25]. Figure 2a displays the IR spectra of our Mn and Mn–Ce samples. Since the IR bands of the MnO_x species are shadowed by those of the support (SiO_2), the spectrum of SiO_2 is given for comparison, as well. The bands of different manganese oxides and those of mono-component manganese and bi-component Mn–Ce catalyst are presented in Table 2. CeO_2 does not show IR bands in this region. According to Julien et al. [25], the FTIR spectra of β-MnO_2 have relatively sharp peaks at 618, 626, and 545 cm^{-1}. The last one has been attributed to the vibration due to the oxygen anions displacement relative to the manganese ions along the direction of the octahedral chains [25]. The specific fingerprints of the vibration features of β-MnO_2 are the well-defined and intense far-infrared bands at 329 and 387 cm^{-1}, which are attributed to vibrations perpendicular to the octahedral chains [25]. The main IR characteristics of the ramsdellite structure (R-MnO_2) are the strong bands at 740 and 687 cm^{-1}. As can be seen from Fig. 2a and Table 2, the IR spectrum of our mono-component manganese sample displays the bands typical for β-MnO_2 and R-MnO_2. Most probably, the mono-metallic Mn catalyst is constituted by β-MnO_2 and amorphous R-MnO_2. The occurrence of β-MnO_2 is visible from XRD data. The fact that XRD pattern characteristic for R-MnO_2 is missing in the diffractogram of Mn sample (Fig. 1), but bands for R-MnO_2 are seen in the IR spectrum give us the reason to suppose that part of manganese oxide is in a form of amorphous R-MnO_2. The low resolved bands at 592, 536, and 670 cm^{-1} in the IR spectrum of Mn–Ce sample could be assigned to Mn_2O_3 oxides since bands with same position are reported as characteristic for Mn_2O_3 [25] (Table 2). The occurrence of Mn_2O_3 is evident from the peak at $2\theta = 33°$ in the XRD spectra of Mn–Ce sample.

Fourier transform infrared spectroscopy spectrum of bi-component catalyst of Mn modified with Co is presented in Fig. 2b. Two wide bands were registered at 567 cm^{-1} (ν_1) and at 658 cm^{-1} (ν_2). The former band is attributed to the stretching vibration of Co^{3+}–O, where Co^{3+} is in octahedral position, and the latter one to the stretching

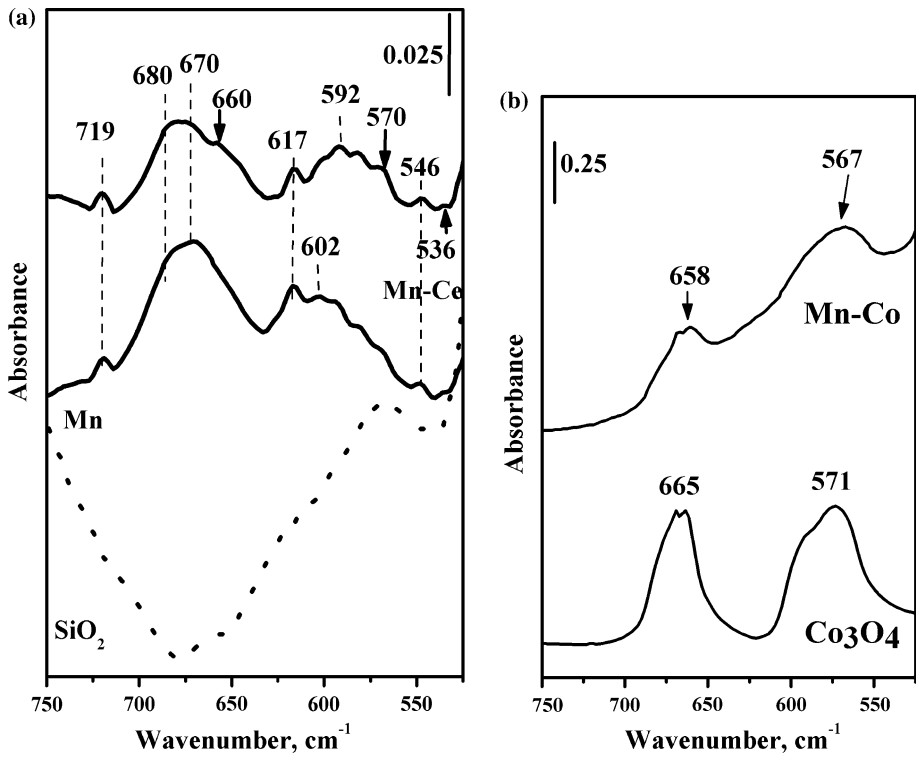

Fig. 2 Infrared spectra of mono-component manganese and bi-component samples: **a** Mn–Ce and **b** Mn–Co calcined at 450 °C

Table 2 IR frequency vibrations of manganese oxides

Samples	IR bands (cm^{-1})						References
Mn	719	670	617	602		546, 335	Present study
Mn–Ce	719	680, 670, 660	617		592, 580, 536	546	Present study
β-MnO_2			618, 626			545	[25]
R-MnO_2	740	687			589, 515		[25]
α-Mn_2O_3				606	576, 533		[25]
γ-Mn_2O_3		666			592, 533		[25]

vibration of Co^{2+}–O, where Co^{2+} is in tetrahedral position [26]. The appearance of these bands could be considered as evidence for the formation of cobalt spinel. The IR spectrum of Co_3O_4 is given for comparison, as well. A shift to lower frequency is observed for these two bands in the spectrum of the bi-component Mn–Co sample, indicating a decrease in the strength of the Co–O bond in Co_3O_4.

Figure 3 represents TPR profiles of all samples. The TPR profile of manganese sample exhibits two peaks at 315 and 410 °C and they are attributed to the two steps reduction of MnO_2 [10, 19]. The reduction profiles of bi-component catalysts are more complicated. The reduction takes place at lower temperatures than in the mono-component manganese catalyst. The assignment of the peaks to different MnO_x species or to specific reduction steps for Mn–Ce catalyst is not simple, because the reduction of ceria takes place concurrently. According to Delimaris and Ioanides [12], Mn promotes the reduction of ceria, and reduction of Ce^{4+} to Ce^{3+} occurs along with reduction of the manganese ions. As cobalt and manganese oxides are reduced in the same temperature interval, it is difficult to make a correct assignment of the reduction peaks to the respective oxide phase for Mn–Co catalyst. The appearance of a broader region of hydrogen consumption in the interval 500–700 °C is assumed to be a result of mixed Co–Mn–oxide phase(s) reduction. Our bi-component samples were prepared by impregnation of the support with nitrates and subsequent calcinations at 400 °C. It has been observed that the decomposition of supported mixed Co–Mn nitrates at low temperatures (250–400 °C) often produces finely divided non-stoichiometric spinel $MnCo_2O_{4+\delta}$ [27]. This is a further reason to ascribe the hydrogen consumption above 500 °C in the bi-component samples to the reduction of mixed Co–Mn oxides.

The oxidation state of the surface was examined by XPS analysis. The XPS spectra in the Mn2p region are given in Fig. 4. According to our previous investigations, the

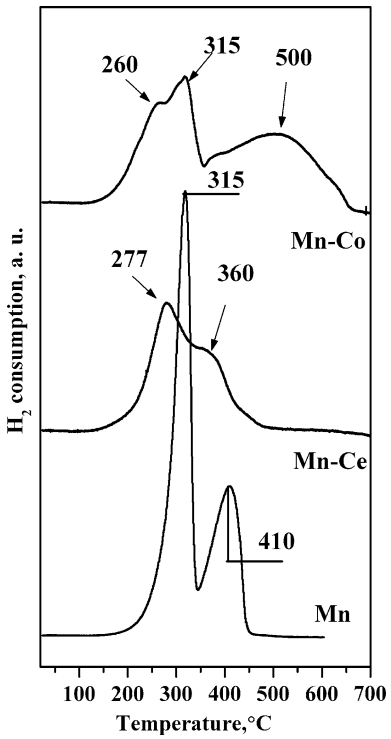

Fig. 3 TPR spectra of mono-component manganese and bi-component catalysts

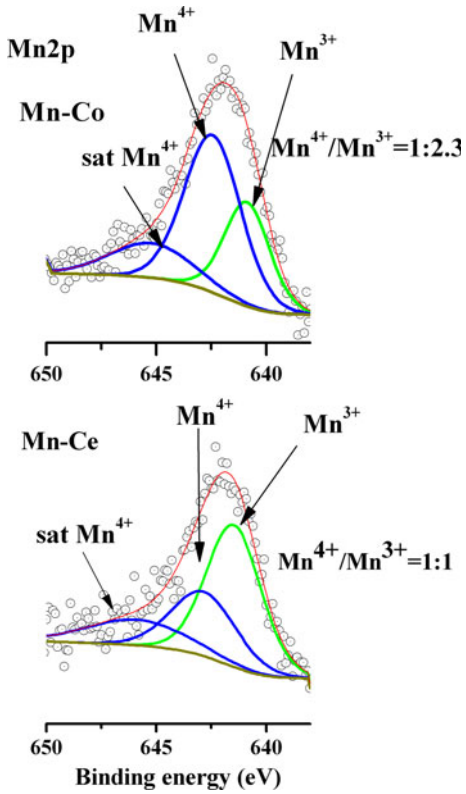

Fig. 4 Fitted Mn2p photoelectron peaks of Mn–Ce and Mn–Co samples

oxidation state of manganese in mono-component sample is Mn^{4+} [10]. Although a general agreement exists in the literature about the binding energy values (BE), associated with the different chemical states of Mn, the identification of various surface species is rather complex in supported samples, because of the small difference in BE shift between the oxidation states and the usual broadness of the peaks. Since the differences between the BE values of Mn^{3+} and Mn^{4+} ions are small, a peak fitting procedure including three components, Mn^{3+}, Mn^{4+}, and a satellite [28–30], was applied. The observed binding energies at 641.5 and 642.9 eV for Mn–Ce and 640.9 and 642.2 eV for Mn-Co are associated with the presence of Mn^{4+} and Mn^{3+} ions, respectively [12, 28–30]. The ratio of Mn^{4+}/Mn^{3+} is 1 and 1/2.3 on the surfaces of Mn–Ce and Mn-Co samples, respectively.

The existence of Mn_2O_3 in the cerium-modified catalysts was proposed based on XRD and FTIR data. Our results are in accordance with Delemaris and Ioanidis [12] who detected Mn_2O_3 in the MnO_x–CeO_2 catalysts prepared by combustion method. The main manganese surface species in Mn–Co sample is Mn^{4+}. The presence of manganese ions in different oxidation states in the bi-component catalysts modified with Co can be explained with the easy formation of solid solutions between cobalt and manganese oxides. The solid-state properties of the title system $Mn_xCo_{3-x}O_4$ have been extensively studied, and mixed oxidation state of cobalt (Co^{2+} and Co^{3+}) and manganese (Mn^{3+} and Mn^{4+}) and various cationic distributions have been proposed depending on the preparation method and the calcination temperature [31, 32]. As can be seen from Table 1, the atomic percentage of manganese is similar for all studied samples, but there is a difference in the cation distribution. The Mn^{4+} and Mn^{3+} ions are in equal quantity on the surface of Mn–Ce catalyst, Mn^{4+} is predominant species for cobalt-modified samples and only Mn^{4+} is detected in the mono-component catalyst [10]. The lower Mn/Ce ratio at the surface than in the bulk is probably due to enrichment in Ce of the surface. The energy positions of the Ce3d peaks and the presence of a peak at BE 916.5 eV correspond to Ce^{4+} in CeO_2 [33], suggesting that the manganese ions does not affect the oxidation state of cerium.

Figure 5 displays XPS spectra in the Co2p region of Mn–Co sample. The spectrum of mono-component Co/SiO_2 catalyst is given for comparison as well. The XPS spectrum of Co sample was fitted assuming Co^{2+}/Co^{3+} ratio of 1:2. The peak of $2p_{3/2}$ at 779.2 eV and the very low intensity of the 3d → 4 s shake-up satellite peak at 785.2 eV are characteristic of Co_3O_4 [34]. The presence of a peak at 780 eV and a satellite at about 787.6 eV in the photoelectron spectra of the bi-component samples indicate

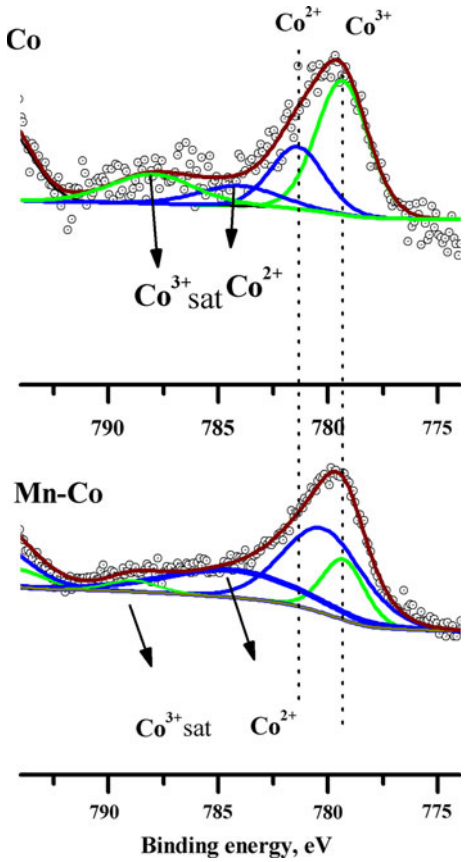

Fig. 5 Fitted Co2p photoelectron peaks of Co and Mn–Co samples

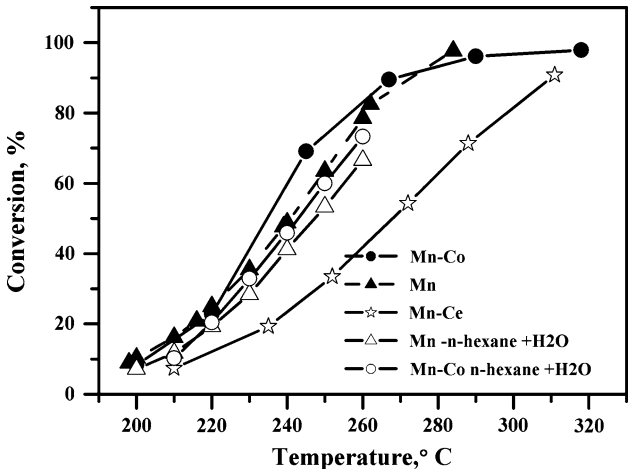

Fig. 6 Temperature dependence of the conversion over all samples in the reaction of complete *n*-hexane oxidation

the presence of Co^{2+} species [35, 36]. As it can be seen from Fig. 5, Co^{2+} is the major species on the surface of these samples.

The temperature dependences of the complete oxidation of *n*-hexane and ethyl acetate over the mono- and bi-component catalysts are shown in Figs. 6 and 7. The combustion of *n*-hexane is more difficult, as it is visible

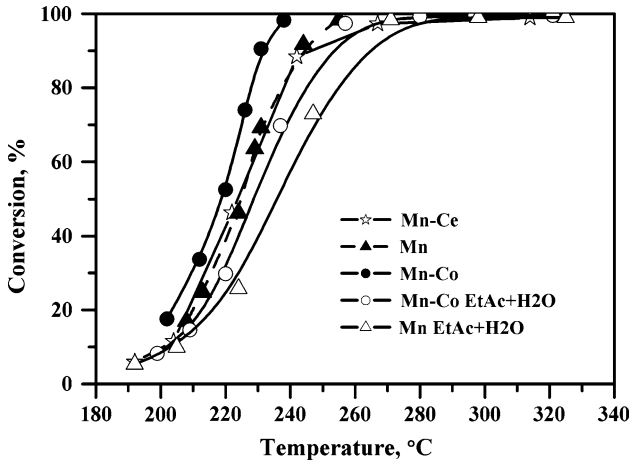

Fig. 7 Temperature dependence of the conversion over all samples in the reaction of complete oxidation of ethyl acetate

from the differences in the temperature intervals of the corresponding S-curves. This result is in accordance with literature data [36] which report difficult oxidation of the saturated hydrocarbons. The temperature of 50% conversion was used as a criterion for the catalytic activity. H_2O and CO_2 were the main detectable reaction products on all investigated samples, while CO was the only product of incomplete oxidation and was in the limits corresponding to conversion of 5% of the inlet VOC.

As it is seen from the Figs. 6 and 7, the rows of activity in the reaction of *n*-hexane and ethyl acetate (EtAc) combustion are: Mn–Co > Mn > Mn–Ce and Mn–Co > Mn ≈ Mn–Ce, respectively. Obviously, the combustion activity is increased in the samples modified with cobalt and is decreased after cerium addition. It is known that the transition metal oxides can operate in the oxidation reactions through a Mars van Krevelen mechanism [37]. According to this mechanism, the substrate is oxidized by the solid. The oxygen species introduced in the substrate come from the lattice. In this way, the catalytic behavior can be correlated to the lattice oxygen mobility of the crystalline framework. The lattice oxygen mobility is associated with the catalyst reducibility [38–40]. As it is discussed above, finely divided oxide particles are formed to a large extent in the Mn–Co and Mn–Ce samples, and, as a consequence, the reducibility of the oxide phase is enhanced. In order to study the role of the lattice oxygen in the mechanism of *n*-hexane oxidation, tests without oxygen in the feed, so-called "depletive" oxidation experiments [41, 42], were performed. The experiment consisted of measuring the formation of oxidation products (CO and CO_2) when the supply of oxygen to the gas mixture was stopped, after attaining steady state at the temperature of 42–44% conversion. The amount of CO + CO_2 formed during the test was calculated from the area under the

transient curves after stopping the oxygen supply to the gas feed. The lattice oxygen, which takes part in the reaction, was calculated on the basis of formed carbon oxides quantities. The duration of the experiment was limited to 150 min, since the oxidation process was practically accomplished on all samples. The amounts of consumed oxygen were 7 mg for Mn–Co, 12 mg for Mn, and 5 mg for Mn–Ce samples. Therefore, the largest quantity of oxygen withdrawn from the lattice was obtained with the pure manganese catalyst. The quantity of lattice oxygen, which interacted with *n*-hexane during "depletive" oxidation, was lowest for cerium-modified catalyst. This result is in accordance with the lower activity of cerium-modified catalyst, providing evidence that the lattice oxygen is responsible for the catalytic performance.

The results presented on Figs. 6 and 7 show that Mn–Co sample exhibits higher activity in both combustion reactions. This can be explained by synergy effect of Mn and Co oxides because both of them are active in oxidation reactions. Obviously, the highest activity of Mn–Co sample could not be correlated only with lattice oxygen mobility, since the quantity of withdrawn oxygen for Mn–Co is lower than for mono-component manganese catalyst. Probably, additional factors such as the simultaneous presence of Mn^{4+}–Mn^{3+} couple, the decrease in the strength of Co–O bond (as is seen from IR spectrum), and the predominance of Co in the second oxidation state on the catalyst surface are responsible for the higher catalytic activity of Mn–Co. It was established that catalytic activity increased when the pair Mn^{4+}–Mn^{3+} existed in the structure of the oxide [43]. As was shown by XPS data, Co in the bi-component sample was mainly in the form of Co^{2+}. Co^{2+} ion, located at a relatively opened coordination position on the support, can be a center of oxygen adsorption and formation of active oxygen species, which are a prerequisite for catalytic oxidation [44]. It is worth to note that the enhanced reducibility upon combination of Mn and Ce oxides (as inferred by TPR results) is not translated into a higher activity in *n*-hexane and ethyl acetate oxidation. According to literature data, the composition of Mn–Ce catalyst and the interaction between MnO_x and CeO_2 strongly affected the catalyst activity [6, 7, 11]. The optimum composition was found to depend on the nature of the pollutant to be destroyed and the method of preparation [11, 21, 45]. Most probably, the current Mn–Ce catalyst has no optimum composition for *n*-hexane oxidation, and for improved performance in *n*-hexane oxidation, an optimization procedure should be applied with the current Mn–Ce composition. The enrichment in cerium of the surface (as was shown with XPS data in Table 1) and the lower lattice oxygen mobility could be factors responsible for the poor catalytic activity in *n*-hexane combustion. In the case of ethyl acetate oxidation, the mono-component manganese and the cerium-modified samples exhibit the same activity. We established in previous investigations (unpublished data) that twofold increase in the concentration of manganese in the catalyst does not change the catalytic activity in ethyl acetate oxidation. These results were attributed to the similar Mn/Ce ratio on the surface (1.15 and 1.16, respectively).

The performance of the most active bi-component Mn–Co catalyst was also examined in the presence of H_2O in the VOC/air feed, as this compound is commonly found in typical VOC-containing exhaust streams. The presence of water (1.0 vol.%) resulted in decreased conversion over all studied catalysts (Figs. 6, 7). Mn–Co sample is more sensitive in comparison with mono-metallic manganese catalyst in the case of *n*-hexane oxidation. The presence of water in the inlet mixture has more noticeable effect on the ethyl acetate combustion, as seen by the shift of S-curves to the higher temperatures with about 10 °C at T_{50}. This effect is ascribed to the competitive adsorption of organic molecule and water molecule on the catalytic active sites [46].

Conclusions

The preparation of supported oxide catalysts combining manganese with cobalt or cerium by impregnation of silica with solution containing both components leads to the formation of finely divided oxide particles and, as a consequence, to the enhancement of the reducibility of the oxide phase(s).

Mn^{4+} and Mn^{3+} ions were found on the surface of Mn–Ce and Mn–Co samples. Mn^{4+} and Mn^{3+} are equally represented on the surface in Mn–Ce catalyst; Mn^{4+} is the predominant species in cobalt-modified sample and only Mn^{4+} is detected in mono-component catalyst. The addition of Co to the manganese catalyst leads to partial dissolution of cobalt in the lattice of MnO_2 and formation of mixed oxide phases. Cobalt is predominantly in the second oxidation state (Co^{2+}) on the surface.

The better catalytic performance of the Mn–Co sample in both studied combustion reactions is correlated with the higher lattice oxygen mobility, the simultaneous presence of Mn^{4+}–Mn^{3+} couple, the decrease in strength of the Co–O bond, and the predominance of Co in the second oxidation state on the catalyst surface. The poor catalytic activity of the cerium-modified catalyst is related to the predominance of Ce on the surface and the lower lattice oxygen mobility.

Acknowledgements A. Naydenov and G. Ivanov gratefully acknowledge the financial support by the National Science Fund of Bulgaria (National Centre for New Materials UNION, Contract No DO-02-82/2008).

References

1. Li WB, Wang JX, Gong H (2009) Catal Today 148:81
2. Craciun R, Nentwick B, Hadjiivanov K (2003) Appl Catal A 243:67
3. Craciun R (1998) Catal Lett 55:25
4. Thormählen P, Skoglundh M, Fridell E, Anderson B (1999) J Catal 188:300
5. Cunningham DAH, Kobayashi T, Kamijo N, Haruta M (1994) Catal Lett 25:257
6. Chai KS (2002) J Hazard Mater 91:285
7. Papaefthiniou P, Ioannides T, Verykious XE (1997) Appl Catal B 13:175
8. Milt VG, Ulla MA, Lombardo EA (2001) J Catal 200:241
9. Torncrona A, Skoglundh M, Thormählen P, Fridell E, Jobson E (1997) Appl Catal B 14:13
10. Todorova S, Kolev H, Holgado JP, Kadinov G, Bonev Ch, Pereñíguez R, Caballero A (2010) Appl Catal B 94:46
11. Rao T, Shen M, Jia L, Hao J, Wang J (2007) Catal Commun 8:1743
12. Delimaris D, Ioanides T (2008) Appl Catal B 84:303
13. Picasso G, Gutierrez M, Pina MP, Herguido J (2007) Chem Eng J 126:119
14. Zhecheva E, Stoyanova R, Tyuliev G, Tenchev K, Mladenov M, Vassilev S (2003) Solid State Sci 5:711
15. Kanungo SB (1979) J Catal 58:419
16. Parida KM, Kanungo S (1983) Thermochim Acta 64:131
17. Gil A, Gandía LM, Korili SA (2004) Appl Catal A 274:229
18. Lamaita L, Peluso M, Sambeth JE, Thomas HJ (2005) Appl Catal B 61:114
19. Arena F, Torre T, Raimondo C, Parmaliana A (2001) Phys Chem Chem Phys 3:1911
20. Shi L, Chu W, Qu F, Luo S (2007) Catal Lett 113:59
21. Chen H, Sayari A, Adnot A, Larachi F (2001) Appl Catal B 32:195
22. El-Shobaky HG, Shouman MA, Attia AA (2006) Colloid Surf A 274:62
23. Morales F, Grandjean D, de Groot FMF, Stephanb O, Weckhuysen BM (2005) Phys Chem Chem Phys 7:568
24. Kanga L, Zhang M, Liu Z-H, Ooi K (2007) Spectrochim Acta A 67:864
25. Julien CM, Massot M, Poinsignon C (2004) Spectrochim Acta A 60:689
26. Lefez B, Nkeng P, Lopitau J, Poillerat G (1996) Mater Res Bull 3:1263
27. Nissinen T, Leskel M, Gasik M, Lamminen J (2005) Thermochim Acta 427:155
28. Ponce S, Pena MA, Fierro JLG (2000) Appl Catal B 24:193
29. Zhang-Steenwinkel Y, Beckers J, Bliek A (2002) Appl Catal A 235:79
30. Machocki A, Ioannides T, Stasinska B, Gac W, Avgouropoulos G, Delimaris D, Grzegorczyk W, Pasieczna S (2004) J Catal 227:282
31. Bazuev GV, Korolyov AV (2008) J Magn Magn Mater 320:2262
32. Rios E, Gautier J-L, Poillerat G, Chartier P (1998) Electrochim Acta 44:1491
33. Larachi F, Pierre J, Adnot A, Bernis A (2002) Appl Surf Sci 195:236
34. Shanke D, Vada S, Hilmen EA, Hoff A (1995) J Catal 156:85
35. Allen GC, Hallam KR (1996) Appl Surf Sci 93:25
36. Palazzolo MA, Tichenor BA (1987) Environ Prog 6:172
37. Vedrine JC, Coudurier G, Millet J-MM (1997) Catal Today 33:3
38. Li JJ, Xu XY, Hao ZP, Zhao W (2008) J Porous Mater 15:163
39. Finocchio E, Busca G, Lorenzelli V, Sanchez Escribano V (1996) J Chem Soc Faraday Trans 92:1587
40. Solsona B, Davies TE, Garcia T, Vázquez I, Dejoz A, Taylor SH (2008) Appl Catal B 84:176
41. Brooks CS (1967) J Catal 8:272
42. Bastos SST, Órfão JJM, Freitas MMA, Pereira MFR, Figueiredo JL (2009) Appl Catal B 93:30
43. Figueroa SJA, Requejo FG, Lede EJ, Lamaita L, Peluso MA, Sambeth JE (2005) Catal Today 107–108:849
44. Łojewska J, Kołodziej A, Żak J, Stoch J (2005) Catal Today 105:655
45. Azalim S, Franco M, Brahmi R, Giraudon J-M, Lamonier J-F (2011) J Hazard Mater 188:422
46. Abdullah AZ, Zailani M, Bakar A, Bhatia S (2003) Ind Eng Chem Res 42:6059